bioRxiv preprint doi: https://doi.org/10.1101/141150; this version posted May 23, 2017. The copyright holder for this preprint (which was not certified by peer review) is the author/funder, who has granted bioRxiv a license to display the preprint in perpetuity. It is made available under aCC-BY 4.0 International license.

Title:

Postmitotic nuclear pore assembly proceeds by radial dilation of small ER membrane openings

Authors/Affiliations:

Shotaro Otsuka,[1] Anna M. Steyer,[1] Martin Schorb,[3] Jean-Karim Hériché,[1] M. Julius Hossain,[1] Suruchi Sethi,[1] Yannick Schwab,[1,3] Martin Beck,[1,2] Jan Ellenberg[1]*

[1]Cell Biology and Biophysics Unit, European Molecular Biology Laboratory, Meyerhofstrasse 1, 69117 Heidelberg, Germany.

[2]Structural and Computational Biology Unit, European Molecular Biology Laboratory, Meyerhofstrasse 1, 69117 Heidelberg, Germany.

[3]Electron Microscopy Core Facility, European Molecular Biology Laboratory, Meyerhofstrasse 1, 69117 Heidelberg, Germany.

*Corresponding author

Contact: jan.ellenberg@embl.de

bioRxiv preprint doi: https://doi.org/10.1101/141150; this version posted May 23, 2017. The copyright holder for this preprint (which was not certified by peer review) is the author/funder, who has granted bioRxiv a license to display the preprint in perpetuity. It is made available under aCC-BY 4.0 International license.

Abstract:

The nuclear envelope has to be reformed after mitosis to create viable daughter cells with closed nuclei. How membrane sealing of DNA and assembly of nuclear pore complexes (NPCs) are achieved and coordinated is poorly understood. Here, we reconstructed nuclear membrane topology and structure of assembling NPCs in a correlative three dimensional electron microscopy time-course of dividing human cells. Our quantitative ultrastructural analysis shows that nuclear membranes form from highly fenestrated ER sheets, whose shrinking holes are stabilized and then dilated into NPCs during inner ring complex assembly, forming thousands of transport channels within minutes. This mechanism is fundamentally different from interphase NPC assembly and explains how mitotic cells can rapidly establish a closed nuclear compartment while making it transport-competent at the same time.

bioRxiv preprint doi: https://doi.org/10.1101/141150; this version posted May 23, 2017. The copyright holder for this preprint (which was not certified by peer review) is the author/funder, who has granted bioRxiv a license to display the preprint in perpetuity. It is made available under aCC-BY 4.0 International license.

Introduction:

The nuclear pore complex (NPC) is the largest non-polymeric protein complex in eukaryotic cells and composed of multiple copies of around 30 different proteins termed nucleoporins (Nups) (Beck and Hurt, 2017). NPCs are the sole gates of macromolecular transport across the double membrane of the nuclear envelope (NE). In higher eukaryotes, NPCs and the NE disassemble at the beginning of mitosis and their rapid reformation during mitotic exit is essential for establishing a functional nucleus in the daughter cell (Weberruss and Antonin, 2016; LaJoie and Ullman, 2017; Ungricht and Kutay, 2017).

The process of postmitotic assembly of the NPC and the nuclear membranes from mitotic ER has been studied *in vitro* using nuclei assembled in *Xenopus* egg extract and by live cell imaging using fluorescence microscopy. Several molecular players regulating the process have been identified, including inner nuclear membrane proteins, ER shaping proteins such as reticulons, nuclear pore components ELYS and Nup107–160 complex, nuclear transport receptors and Ran (Weberruss and Antonin, 2016; LaJoie and Ullman, 2017; Ungricht and Kutay, 2017). In addition, kinetic observations of the bulk NPC formation across the NE has shown that postmitotic assembly proceeds by sequential addition of Nups in a clear temporal progression, that is almost identical between rodent and human cells (Dultz et al., 2008; Otsuka et al., 2014).

Despite these important insights, the mechanism of NPC assembly after mitosis has remained unclear and is highly debated (Rabut et al., 2004; Antonin et al., 2008; Wandke and Kutay, 2013; Schellhaus et al., 2015). Whether postmitotic NPC assembly is initiated in an already sealed NE and the NPC is inserted into this double membrane by a *de novo* fusion event (Fichtman et al., 2010; Lu et al., 2011) similar to NPC assembly during interphase (Otsuka et al., 2016), or if it starts already on the naked DNA and the membrane only later engulfs assembling NPC from the side (Walther et al., 2003; Rotem et al., 2009), has remained unanswered. How thousands of NPCs can assemble within a few minutes without interfering with the rapid sealing of NEs during mitotic exit thus has remained mysterious. A major reason for this gap in our knowledge was that individual NPCs and ER topology are below the resolution of live cell fluorescence microscopy that is needed to capture the dynamic process of postmitotic nuclear assembly, as well as the unphysiological nature of the *in vitro* nuclear reconstitution system with *Xenopus* egg extract, precluding reliable and quantitative observation of NPC assembly and the sealing of NE membranes. Here, we combine live cell imaging with high resolution 3D electron microscopy to ultrastructurally reconstruct the dynamic process of postmitotic NPC and NE assembly.

bioRxiv preprint doi: https://doi.org/10.1101/141150; this version posted May 23, 2017. The copyright holder for this preprint (which was not certified by peer review) is the author/funder, who has granted bioRxiv a license to display the preprint in perpetuity. It is made available under aCC-BY 4.0 International license.

Results:

Nuclear membranes form from highly fenestrated ER sheets

To measure how nuclear membrane sealing around DNA relates to NPC formation in space and time, we reconstructed whole dividing human cells with a time resolution of approximately one minute after the beginning of mitotic chromosome segregation by correlating single cell live imaging with focused ion beam scanning electron microscopy (FIB-SEM) (Figs. 1A, S1). Segmentation of membranes in proximity to chromosomes showed that the mitotic ER forms highly fenestrated sheets (Fig. 1B, C, Movie S1) as reported previously (Puhka et al., 2012). At early times only about 10% of the chromosome surface was associated with ER, but starting at about 5 min after anaphase onset (AO), the surface of ER-chromosome contacts increased rapidly covering the chromosomes with newly formed NE within 2 min (Fig. 1B, D, Table S1). Fine 3D segmentation of ER/NE membranes (Movie S2) in the large volume EM data showed that at early times (up to 3.9 min) the ER sheets contacting chromosomes had a high degree of fenestration, with variably sized holes making up 43% of their surface (Fig. 1C, E) and 59% of these discontinuities displaying a diameter below 100 nm (Fig. 1F), on the order of NPCs. The degree of fenestration and hole size in the ER sheets contacting chromosomes decreased rapidly (Fig. 1C), with holes making up 16% of the surface two minutes later and now 75% of them having a diameter below 100 nm (Fig. E, F; 6.3 min). This data demonstrates that the NE forms from highly fenestrated ER sheets that contain a very large number of discontinuities whose diameter shrinks as NE assembly proceeds.

Coverage of chromosomes by nuclear membranes is closely linked to pre-pore formation

As ER fenestrae started to shrink significantly as early as 4.3 min after AO (Fig. 1F), many of the pore sized discontinuities started to contain electron dense material (Fig. 1A–C, Table S1) and could therefore be classified as pre-pores. From their first appearance, the number of such pre-pores increased rapidly to 2000 within only 3 min (Fig. 1D). Kinetic analysis of chromosome coverage by newly forming NEs and the appearance of pre-pores showed that both processes display sigmoidal kinetics and are closely linked in time with pre-pore appearance reaching its half-maximum within less than one minute after chromosome coverage (Fig. 1D).

NPC assembly proceeds by dilation of small membrane holes

Knowing when exactly pre-pores start to form during NE formation, enabled us to examine the architecture of assembling NPCs at an even higher resolution. We performed correlative live

bioRxiv preprint doi: https://doi.org/10.1101/141150; this version posted May 23, 2017. The copyright holder for this preprint (which was not certified by peer review) is the author/funder, who has granted bioRxiv a license to display the preprint in perpetuity. It is made available under aCC-BY 4.0 International license.

imaging with electron tomography, in cells captured every 1–2 min after AO (Fig. 2A, Movie S3), starting at 4.8 min when pre-pores first appear (Fig. 1D) until 15 min when NE formation is completed (Fig. 1B, D). Since NE sealing is delayed in the so called 'core-regions' due to clearance of dense spindle microtubules (LaJoie and Ullman, 2017) (Fig. 1B), we focused our analysis on the non-core regions of the NE (Fig. 2A). In a total of 27.8 μm^2 reconstructed NE surface area, we identified 360 particles consistent with pre-pores (i.e. displaying a NE discontinuity containing electron dense material) captured at different times of postmitotic assembly (Figs. 2B, S2A, Table S2). At early times we also found 50 similarly-sized NE discontinuities without internal dense material, that we classified as empty NE holes (Fig. S3).

We first focused our analysis on changes in NE topology. Tracing of the pre-pore membrane profiles in the 3D tomograms and their quantitative analysis revealed that pre-pore diameter increased rapidly from 39 nm (4.8 min after AO) to 63 nm (10.2 min) at which size they stabilized (Fig. 2B, C). The profile analysis also revealed other interesting NE topology changes (Fig. S2B, C). The pre-pore dilation showed sigmoidal kinetics, reaching its half-maximum within 1.2 min after pre-pore appearance (Figs. 1D, 2C), predicting that it represents a maturation step into fully assembled NPCs. Detailed analysis of the distribution of pre-pore diameters at different postmitotic times allowed classification into two groups, smaller and larger pre-pores with a mean diameter of 42 and 62 nm, respectively (Fig. S4). As predicted, the combined abundance of smaller and larger pre-pores matched the number of mature NPCs found after completion of nuclear reformation (Figs. 2D, S5, Table S2). Interestingly, at the beginning of pre-pore appearance (4.8 min), the slightly lower than expected density of smaller pre-pores was made up by the presence of similarly sized empty NE holes, which disappeared at later times (Fig. 2D). Overall, this data indicates that pre-pores mature by membrane hole dilation into fully-assembled NPCs and that empty NE holes are likely to be precursors of pre-pores that have not yet accumulated a significant amount of dense material.

NPC assembly proceeds by centrifugal formation of a membrane associated ring

We next analyzed how the distribution of dense material inside the pre-pores changes during their maturation. We first radially averaged all density inside the membrane hole in the NE plane of pre-pores (Fig. 3A). The change in mean radial intensity profiles over time showed that initially (4.8 min), pre-pores contained material in the center of the membrane hole; From 4.8 to 10 min, material progressively accumulated next to the membrane, resulting in a growing intensity peak that was close to the expanding wall of the membrane channel. After this

bioRxiv preprint doi: https://doi.org/10.1101/141150; this version posted May 23, 2017. The copyright holder for this preprint (which was not certified by peer review) is the author/funder, who has granted bioRxiv a license to display the preprint in perpetuity. It is made available under aCC-BY 4.0 International license.

peripheral accumulation of material, the center of the channel accumulated additional density from 10 min to interphase, leading to a second central peak in the radial profiles (Figs. 3A, S6).

Subtomogram averaging revealed a clear structural maturation of pre-pores

To obtain better insight into the structural changes during NPC assembly, subtomogram averaging of single pre-pores in the same state of assembly is necessary. Since the distributions of membrane hole diameters and profiles of dense material indicated that individual pre-pores sampled at the same time-point can vary in structure (Figs. S4, S6), we ordered them independent of time based on structural similarity using spectral seriation (Fig. 3B, C). Such spectral ordering of pre- and mature pores overall recapitulatedtheir temporal sampling during anaphase, with pores at early (4.8 and 6.1 min), middle (7.7 min), and late (10, 15 min and interphase) time points ranked together (Figs. 3C, S7), showing that postmitotic NPC assembly is indeed a progressive process. Based on their structural similarity, we partitioned pores into five assembly states (Fig. S7) and performed subtomogram averaging. The averages revealed a striking progression of structural changes during postmitotic NPC assembly (Fig. 4A). Early and smaller pre-pores (cluster 1), exhibited dense material in the center of a narrow membrane gap, which subsequently shifted centrifugally towards the membrane (cluster 2) and then dilated into a clear peripheral ring with a first sign of the 8-fold rotational symmetry of the NPC inner ring complex (cluster 3). Inner ring complex formation was then completed with clear 8-fold symmetry (cluster 4), which was followed by maturation of the central channel density (cluster 5, Fig. 4A). Below the double nuclear membranes, density consistent with the nuclear ring was present from the beginning (cluster 1), whereas cytoplasmic ring-like density above the NE appeared only later (cluster 3, Fig. 4A). The same order of inner ring formation and dilation on top of an early assembled nucleoplasmic ring, followed by cytoplasmic ring assembly and central channel maturation, was also observed if pre-pores were clustered only according to experimental time (Fig. S8A, B), showing that the pore maturation process is largely synchronous. Analysis of the increase in inner ring complex intensity over time in time-clustered averages furthermore showed that its sigmoidal rise coincides with the process of membrane dilation (Fig. S8C).

Discussion:

How thousands of NPCs assemble into the reforming NE during mitosis exit has remained unclear due to the resolution limitation of conventional microscopy typically used to observe this dynamic process. Our temporally-staged ultrastructural analysis for the first time resolved

bioRxiv preprint doi: https://doi.org/10.1101/141150; this version posted May 23, 2017. The copyright holder for this preprint (which was not certified by peer review) is the author/funder, who has granted bioRxiv a license to display the preprint in perpetuity. It is made available under aCC-BY 4.0 International license.

postmitotic NE and NPC assembly at nanometer resolution, enabling us to formulate a data-driven model of its mechanism (Fig. 4B, C). The fact that ER sheets that form the NE contain a sufficient number of small discontinuities for NPC assembly (Fig. 1), and that we did not observe holes smaller than 20 nm in the NE although our resolution is sufficient to resolve them (Figs. 2, S4), strongly suggests that postmitotic NPC assembly starts in pre-existing NE openings rather than by *de novo* fusion into already sealed double membranes. The assembly process would thus start by stopping ER/NE hole shrinkage at around 30 nm, accumulate protein in the center of the membrane hole and the nuclear ring underneath it, dilate the hole to NPC size of about 60 nm during inner ring formation, and then assemble the cytoplasmic ring and central channel (Fig. 4B, C). This structural progression is consistent with previous observations in live cells that nuclear/cytoplasmic ring components (Nup107 and Nup133) start to accumulate in the NE first, followed by the inner ring component Nup93 (Dultz et al., 2008; Otsuka et al., 2014). The early presence of the nuclear ring suggests that it may play a role in stalling hole shrinkage or starting inner ring formation. The fact that inner ring complex formation and hole dilation occur exactly at the same time with indistinguishable kinetics (Fig. S8C), suggests that inner ring complex self-assembly may drive pore dilation.

This rapid radial dilation mechanism during inner ring complex formation allows assembly of ~2000 postmitotic NPCs in only 3 min during NE sealing after mitosis. This very high efficiency can now be explained, since assembly into the shrinking holes of highly fenestrated mitotic ER sheets does not require the energetically costly membrane deformation and fusion (Shibata et al., 2009), that is needed for the much slower *de novo* assembly of NPCs into intact nuclei (Otsuka et al., 2016). Our finding that the NPC assembles via fundamentally different mechanism in mitosis provides the basis to dissect the structural and regulatory steps that drive assembly, which will help us to understand general principles of how multi-protein complexes self-assemble inside cells and is highly interesting to shed light on their evolutionary origin (Baum and Baum, 2014; Devos et al., 2014).

bioRxiv preprint doi: https://doi.org/10.1101/141150; this version posted May 23, 2017. The copyright holder for this preprint (which was not certified by peer review) is the author/funder, who has granted bioRxiv a license to display the preprint in perpetuity. It is made available under aCC-BY 4.0 International license.

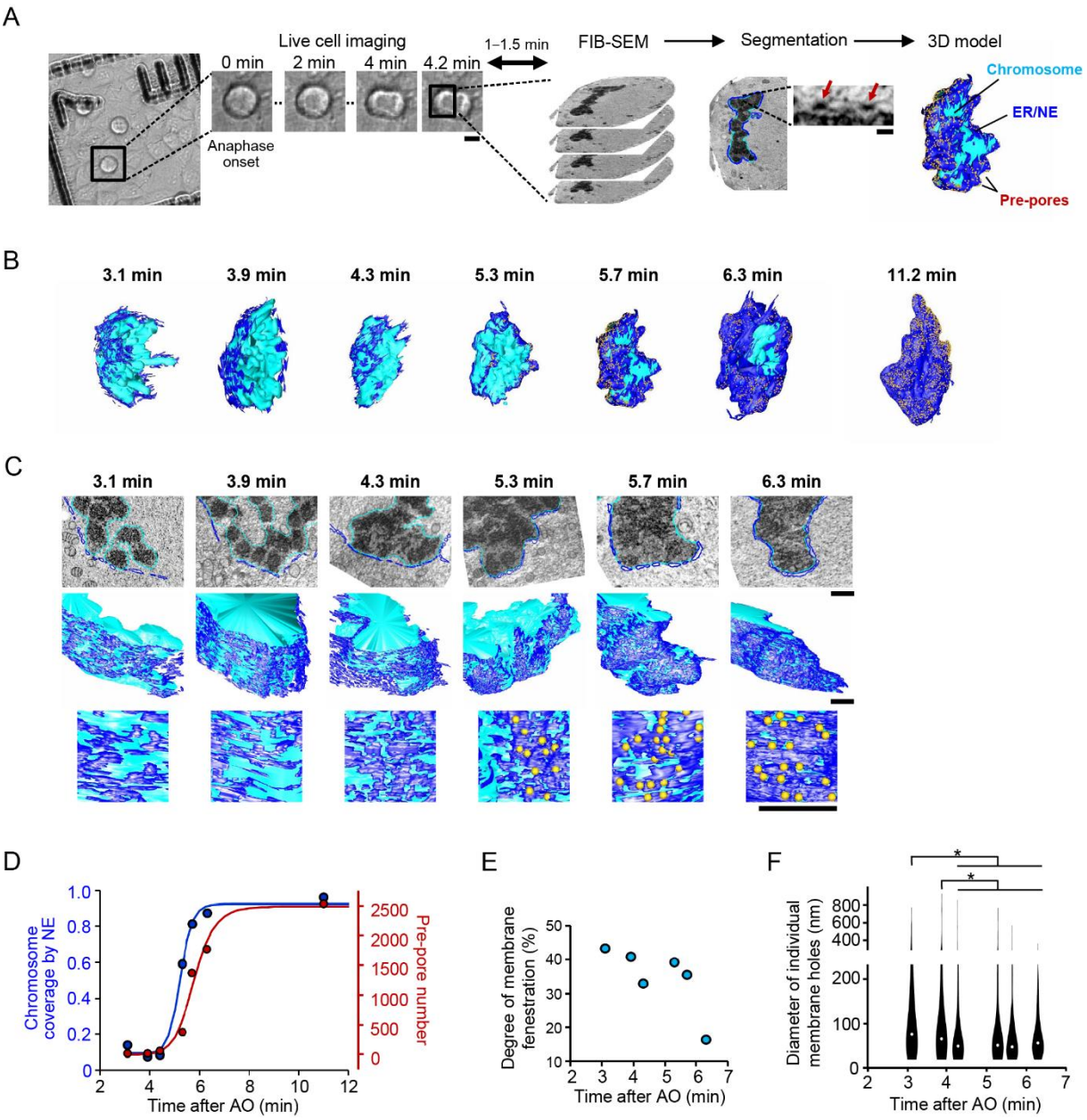

Figure 1. The nuclear envelope (NE) forms from highly fenestrated ER sheets. (A) Correlative live imaging with FIB-SEM. Cell division of HeLa cells was monitored every 0.2 min by light microscopy, and the time from anaphase onset (AO) to the time when the cells were frozen was measured for each cell. The data of 5.7 min cell is shown as an example. Dark red arrows indicate the pre-pores. The chromosome, the ER membranes in proximity to the chromosome, and pre-pores were segmented and shown as a model. Scale bar for LM, 10 μm; for EM 100 nm. (B) Models of entire nuclei at different times after AO. (C) Fine models for the selected parts of the nuclei. Examples for the segmentation, the model overview, and the enlarged view with pre-pores are shown in the upper, middle and lower panels, respectively. Scale bars, 1 μm. (D) Chromosome surface coverage by the NE and the pre-pore number in cells at different postmitotic times. $t_{1/2}$ of the sigmoidal fit for NE sealing and pre-pore appearance were 5.2 and 5.8 min, respectively. (E) The ratio of free space to the membrane on the ER/NE sheet at indicated times. (F) The diameter of membrane holes. The violin plot is from 216, 188, 371, 289, 245, and 202 holes for 3.1, 3.9, 4.3, 5.3, 5.7, and 6.3 min, respectively. The median is depicted as a dot. *$p<0.02$; one-sided Mann-Whitney-Wilcoxon U test with Holm-Bonferroni correction for multiple testing.

bioRxiv preprint doi: https://doi.org/10.1101/141150; this version posted May 23, 2017. The copyright holder for this preprint (which was not certified by peer review) is the author/funder, who has granted bioRxiv a license to display the preprint in perpetuity. It is made available under aCC-BY 4.0 International license.

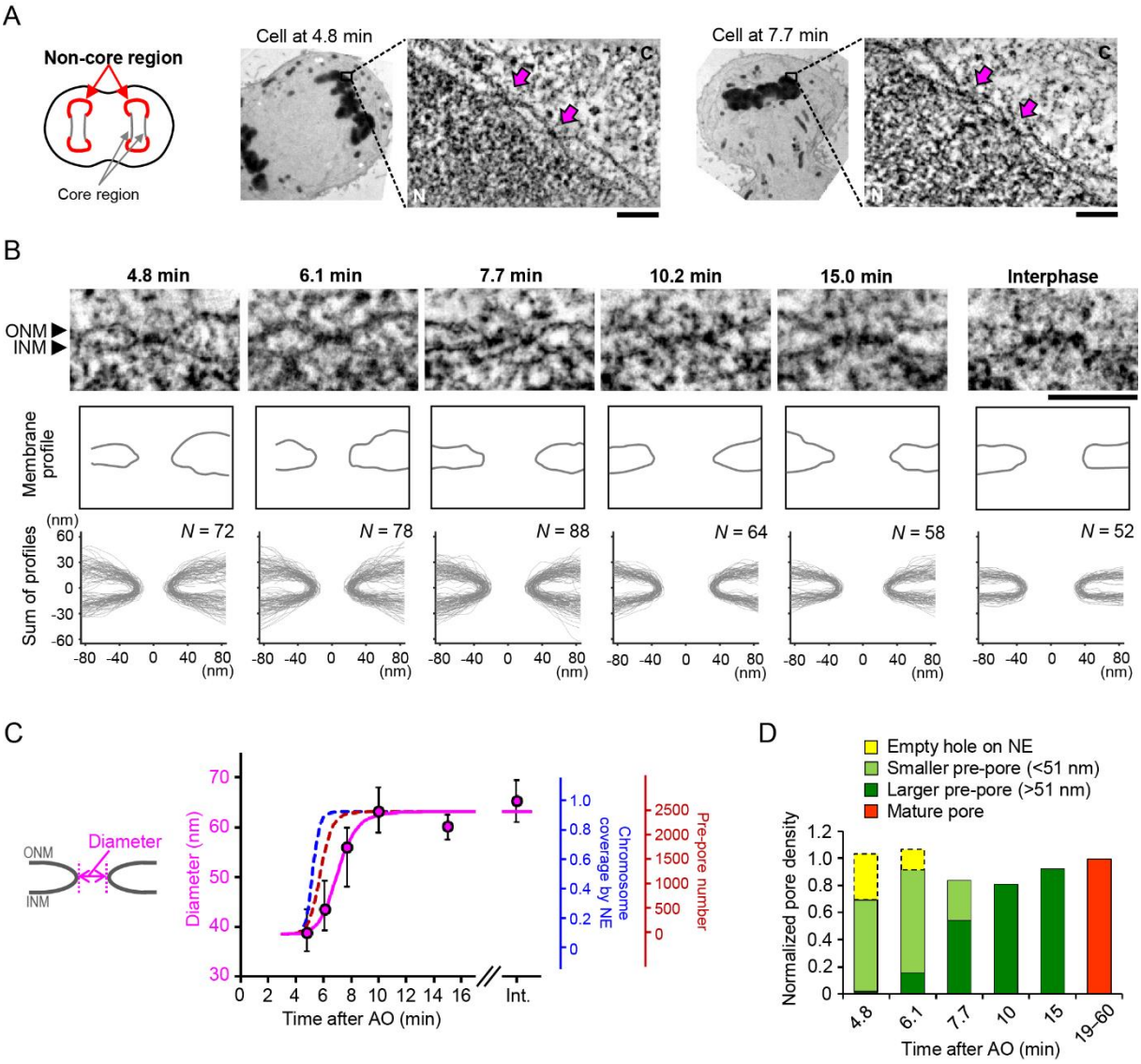

Figure 2. NPC assembly proceeds by dilation of small membrane holes. (A) Electron tomography of non-core regions of the NE (indicated in red in the left panel) in cells captured at different times after AO. Two examples are shown in the right panels. Enlarged images are tomographic slices of the non-core regions of cells at 4.8 and 7.7 min. Pre-pores are indicated by magenta arrows. C, cytoplasm; N, nucleoplasm. Scale bars, 100 nm. (B) Electron tomographic slices of pre- and mature pores at different times after AO. Scale bar, 100 nm. Membrane profiles of the individual pores (middle panels) and all the pores (bottom panels) at each time point are shown. ONM, outer nuclear membrane; INM, inner nuclear membrane. (C) Quantification of the pore diameter as indicated by a bidirectional arrow in the left panel. The median is plotted and the whiskers show the 25th and 75th percentiles, and fitted with a sigmoid function. Sigmoid curves of chromosome coverage by NE and pre-pore number in Fig. 1D are shown by dashed lines for comparison. (D) Normalized density of empty holes on the NE, pre-pores smaller and larger than 51 nm, and mature pores at different times (see Figs. S2–4 for details).

bioRxiv preprint doi: https://doi.org/10.1101/141150; this version posted May 23, 2017. The copyright holder for this preprint (which was not certified by peer review) is the author/funder, who has granted bioRxiv a license to display the preprint in perpetuity. It is made available under aCC-BY 4.0 International license.

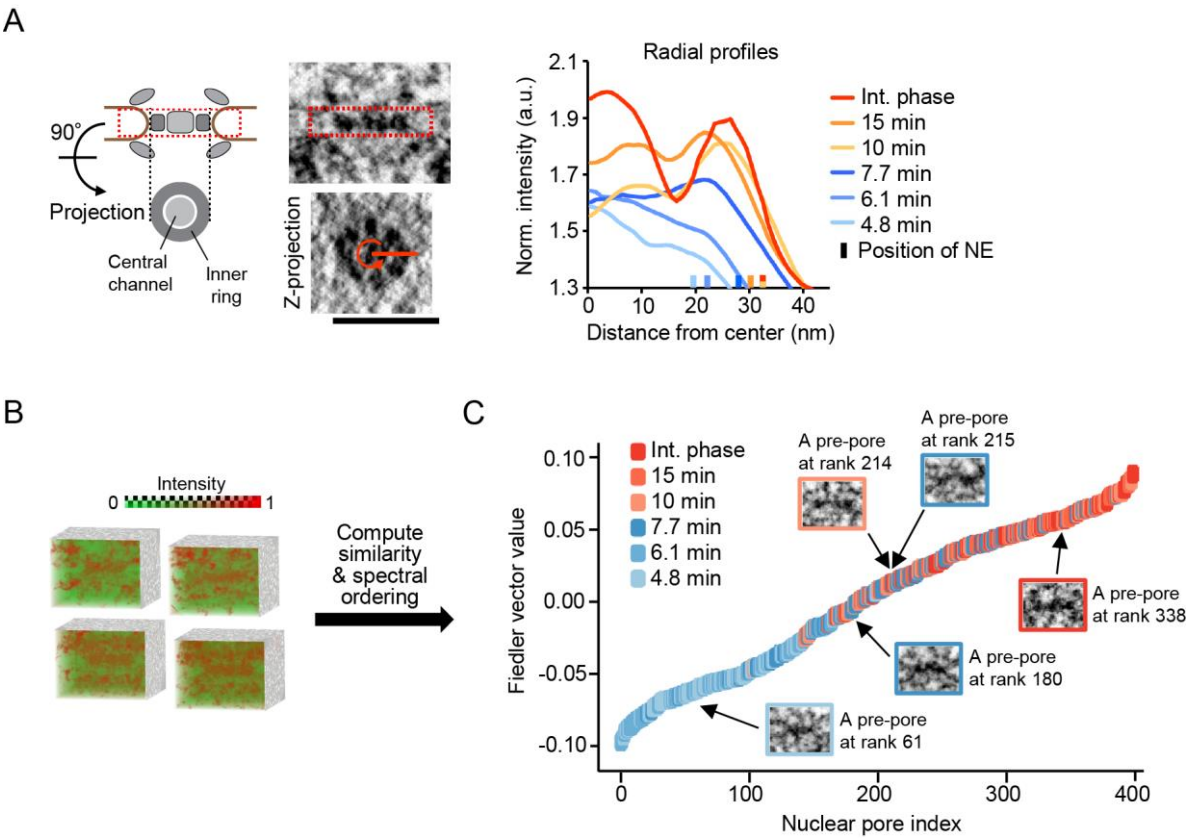

Figure 3. Intensity distribution inside the pre-pore membranes and unbiased classification of pre-pores from spectral ordering. (A) Radial profile analysis of pre-pores. The region indicated by red dashed box in the left panel was Z-projected and the radial intensity from the center of the pore was measured. Intensity was normalized to that of NE lumen. The mean radial intensities for each time point are shown (see also Fig. S6). The positions of the membrane wall are indicated by short lines on the X-axis. Scale bar, 100 nm. (B) 3D intensity distribution of nuclear pores in the electron subtomograms. Four examples are shown. (C) Seriation of nuclear pores. Individual pre- and mature pores were ranked by the Fiedler vector value derived from the similarity of their 3D intensity distributions (see Materials and Methods for details). Individual nuclear pores are color-coded according to their time after AO. Five pores at indicated ranks of are shown as examples.

bioRxiv preprint doi: https://doi.org/10.1101/141150; this version posted May 23, 2017. The copyright holder for this preprint (which was not certified by peer review) is the author/funder, who has granted bioRxiv a license to display the preprint in perpetuity. It is made available under aCC-BY 4.0 International license.

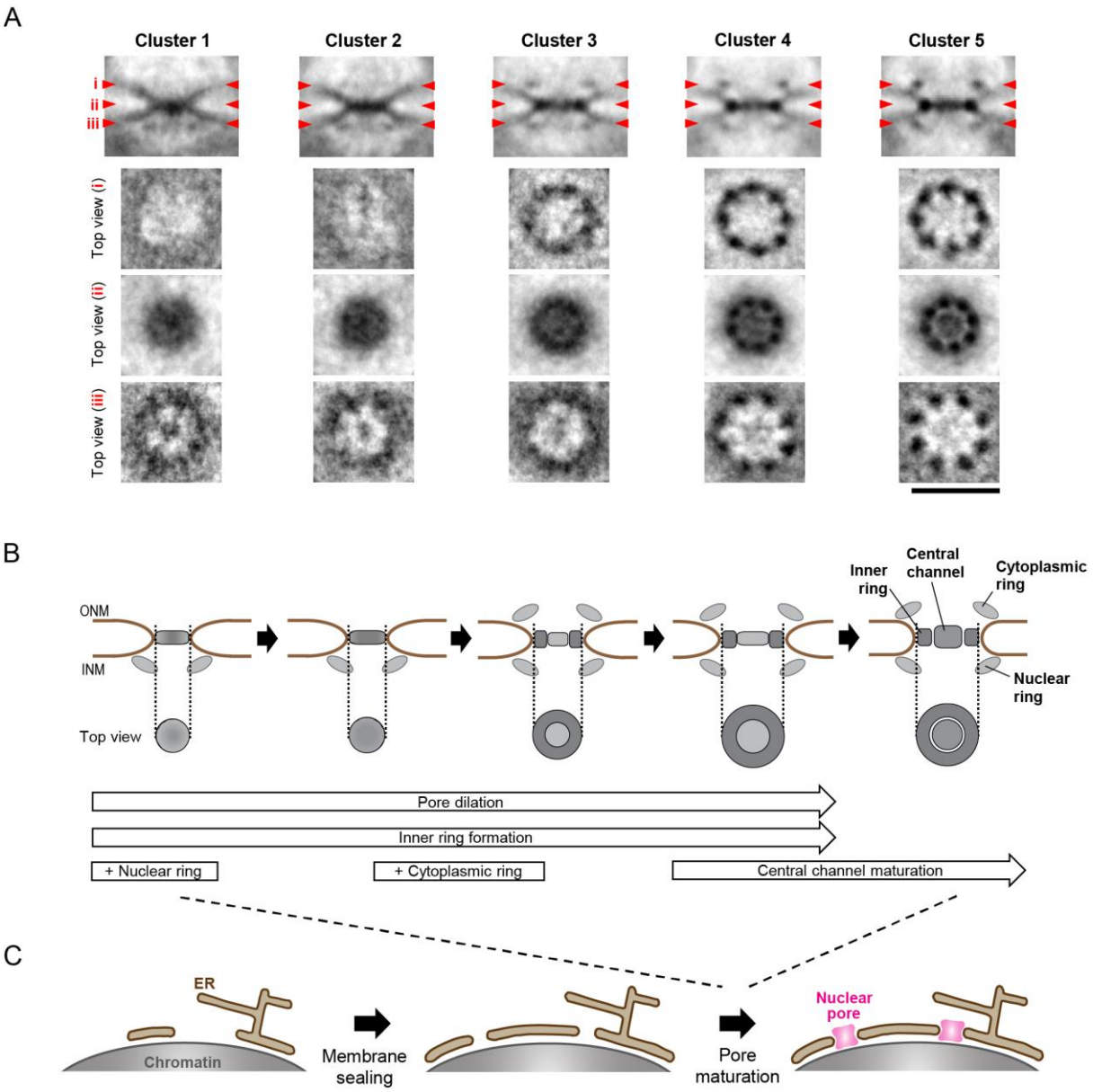

Figure 4. Structural maturation of pre-pores revealed by subtomogram averaging and postmitotic NE/NPC assembly model. (A) Electron tomographic slices of averaged nuclear pores in each cluster. No symmetry was imposed in averaging. The averaged images are from 61, 85, 69, 108, and 76 pores in cluster 1–5. Red arrowheads i, ii, and iii on side-view images indicate the locations of the planes which are inclined at 90° in top views i, ii, and iii. Scale bar, 100 nm. (B) A schematic model of postmitotic nuclear pore assembly. The initial pre-pore consists of some dense material in the center of the pore as well as the nuclear ring. During pore dilation, the inner ring and the cytoplasmic ring form. The pore dilates even further, and then the central channel is filled with additional materials. (C) A schematic model of NE assembly. The NE forms form a highly-fenestrated ER sheet that contains sufficient discontinuities for NPC assembly. The holes on the NE shrink during the membrane sealing, and the NPC assembly is initiated on the pre-existing holes on the NE.

bioRxiv preprint doi: https://doi.org/10.1101/141150; this version posted May 23, 2017. The copyright holder for this preprint (which was not certified by peer review) is the author/funder, who has granted bioRxiv a license to display the preprint in perpetuity. It is made available under aCC-BY 4.0 International license.

Materials and Methods:

Cell culture

Wildtype HeLa kyoto cells (RRID: CVCL_1922; kind gift from Prof. Narumiya in Kyoto University) were grown in Dulbecco's Modified Eagle's Medium (DMEM) containing 4.5 g/l D-glucose (Sigma Aldrich, St. Louis, MO) supplemented with 10% fetal calf serum (FCS), 2 mM l-glutamine, 1 mM sodium pyruvate, and 100 μg/ml penicillin and streptomycin. The mycoplasma contamination was examined by PCR every 2 or 3 months and was always negative. For correlative light–electron microscopy, cells were cultured on sapphire disks (3 mm diameter; Wohlwend GmbH, Sennwald, Switzerland), and for three-dimensional (3D) fluorescence time-lapse imaging, cells were grown on 2-well Lab-Tek Chambered Coverglass (Thermo Fisher Scientific, Waltham, MA).

Sample preparation for electron microscopy

Cells on pattern-branded sapphire disks by carbon-coating were incubated in imaging medium (IM; CO_2-independent medium without phenol red (Invitrogen), containing 20% FCS, 2 mM l-glutamine, and 100 μg/ml penicillin and streptomycin), and the cell division was monitored every 12 sec by widefield microscopy (Axio Observer Z1; Carl Zeiss, Oberkochen, Germany) using 10 × 0.25 NA A-Plan or 20 × 0.4 NA Plan-Neofluar objective (Carl Zeiss) at 37°C in a microscope-body-enclosing incubator. When cells entered the cell-cycle stages of interest, they were immersed in IM containing 20% Ficoll (PM400; Sigma Aldrich) for protecting cells from freezing damage, and then instantly frozen using a high-pressure freezing machine (HPM 010; ABRA Fluid AG, Widnau, Switzerland). It took 1.0–1.5 min from the last time-lapse imaging until the high-pressure freezing, and the time lag was always recorded to precisely determine the duration after anaphase onset. For focused ion beam scanning electron microscopy (FIB-SEM), cells were freeze-substituted into Durcupan resin (Sigma Aldrich) as follows: Frozen cells were incubated with 1.0% osmium tetroxide (OsO_4), 0.1% UA, and 5% water in acetone at -90°C for 20–24 h. The temperature was raised to -30°C (5°C/hour), kept at -30°C for 3 h, and raised to 0°C (5°C/hour). Samples were then washed with acetone, infiltrated with increasing concentrations of Durcupan in acetone (25, 50 and 75%), embedded in 100% Durcupan and polymerized at 60°C for 4 days. For electron tomography, cells were freeze-substituted into Lowicryl HM20 resin (Polysciences Inc., Warrington, PA) as described previously (Otsuka et al., 2016), and sections of 300 nm thickness were cut with an ultramicrotome (Ultracut UCT; Leica, Wetzlar, Germany) and collected on copper–palladium

bioRxiv preprint doi: https://doi.org/10.1101/141150; this version posted May 23, 2017. The copyright holder for this preprint (which was not certified by peer review) is the author/funder, who has granted bioRxiv a license to display the preprint in perpetuity. It is made available under aCC-BY 4.0 International license.

slot grids (Science Services, München, Germany) coated with 1% Formvar (Plano GmbH, Wetzlar, Germany).

Preparation for FIB-SEM acquisition

After high-pressure freezing and freeze-substitution, the sapphire disk was removed with the cells remaining at the surface of the resin block. The block containing the cells was first coarsely trimmed down with a handsaw and then finely with razor blades to make the monolayer cells as parallel as possible to the block-face. To be able to target the cells of interest in the SEM, marks were branded on the surface of the resin disk using a pulsed 20 × 355-nm laser (DPSL-355/14, Rapp Optoelectronic, Hamburg, Germany) coupled in an Olympus CellR widefield microscope using a 20 × 0.7 NA UPlanApo (Olympus) objective with the program called Xcellence cell^frap. The branded pattern left by the carbon coating is visible at the LM. After laser branding of the same landmarks, it is visible on the surface of the sample by the SEM, which can then be used to find back the region of interest (ROI) for image acquisition in the FIB-SEM.

FIB-SEM

The resin disk containing the cells was mounted on a conductive carbon sticker (12 mm, Plano GmbH) that was placed on SEM stubs (6 mm length, Agar Scientific, Stansted, UK). If necessary, the parallel alignment between the disk and the SEM stub was done using small wedges of polymerized Durcupan. To limit charging by the electron beam during SEM imaging, the samples were surrounded by silver paint and coated by gold sputtering for 180 sec at 30 mA in a sputter coater (Q150R S; Quorum Technologies, Laughton, UK). The samples were then introduced into the Auriga 60/Crossbeam 540 (Carl Zeiss) and positioned so that the sample was facing the SEM at an angle of 36° and the FIB at an angle of 54°. ATLAS 3D, part of Atlas5 software (Fibics, Ottawa, Canada), was used to prepare the sample for “Slice & View”. As a first step a protective platinum coat of about 1 µm was deposited using the FIB at 1 nA/700 pA current (for Auriga 60/Crossbeam 540) to protect the surface of the sample and ensure even milling (Narayan et al., 2014). In some datasets tracking lines were milled into the platinum coat with 50 pA FIB current and filled with SiO_2 using 1 nA/700 pA current. An additional layer of platinum was added to protect the marks. The ion beam was used to dig a trench in front of the ROI with 16 nA/15 nA to reach a depth of 30 µm. After these surface modifications, the image surface was polished at 2 or 4 nA/3 nA. For imaging, the FIB was set to 1 or 2 nA/1.5 nA current, and SEM imaging and FIB milling were performed simultaneously (Narayan et al.,

bioRxiv preprint doi: https://doi.org/10.1101/141150; this version posted May 23, 2017. The copyright holder for this preprint (which was not certified by peer review) is the author/funder, who has granted bioRxiv a license to display the preprint in perpetuity. It is made available under aCC-BY 4.0 International license.

2014). The images were acquired at 1.5 kV with the energy selective backscattered (EsB) detector with a grid voltage of 1.1 kV and the analytical mode at 700 pA current (specific for Crossbeam 540). The pixel size in xy was set to be 5 nm and the FIB-milling was done every 8 nm. The dwell time and line average was set for the frame-time to be 1.5 min.

Segmentation of chromosome, ER, nuclear envelope and nuclear pore

The acquired raw FIB-SEM data were aligned using TrackEM2 (Cardona et al., 2012) in ImageJ (http://rsbweb.nih.gov/ij/). After alignment, the stack was cropped, gray levels were inverted and the images were smoothened with a mean filter (kernel size: 15 × 15 nm). For some datasets with stationary noise (mainly vertical stripes), the VSNR (Variational Stationary Noise remover) plugin in ImageJ was used to reduce the effect (Fehrenbach et al., 2012). The full datasets were segmented manually in IMOD (Kremer et al., 1996), whereas some parts of the datasets were segmented semi-automatically in more detail using Ilastik (Sommer et al., 2011) and MIB (Belevich et al., 2016). For the full segmentation in Fig. 1A, B, every 10-15th slices was segmented and the slices in between were interpolated within IMOD. For the detailed segmentation in Fig. 1C, representative parts of the dataset, with the size of 5–10 μm in XY and 2 μm in Z of one set of daughter chromosomes, were selected and segmented every single slices for 3.1, 3.9, 4.3, 5.3, and 6.3 min and every two slices for 5.7 min. The datasets up to 4.3 min, where the ER is not yet firmly attached to the chromosomes, had to be manually segmented in MIB, since the automatic recognition of ER/chromosomes in Ilastik did not perform well. Datasets starting at 5.3 min, where the ER turns into the NE and firmly attaches to the chromosomes, were labeled in the pixel classification pipeline in Ilastik. The different objects were trained on a couple of slices of a dataset and the software predicted on other slices of the dataset. In the end, Ilastik created a simple segmentation file giving the highest probability for each pixel to be foreground (object). The remaining imprecise labelling was removed manually in MIB, and nuclear pores were added in IMOD. For Fig. 1C, the contrast of the FIB-SEM image was enhanced by projection of a series of 2–5 images for presentation purposes.

Quantification of FIB-SEM data

For the analysis of chromosome coverage by the NE, the 3D models of fully-segmented chromosomes and ER were converted to lists of points every 10 pixels in IMOD. The minimal distance from each point on the chromosome surface to ER was measured in 3D space, and the ER within 100 nm away from chromosome surface was defined as the NE.

bioRxiv preprint doi: https://doi.org/10.1101/141150; this version posted May 23, 2017. The copyright holder for this preprint (which was not certified by peer review) is the author/funder, who has granted bioRxiv a license to display the preprint in perpetuity. It is made available under aCC-BY 4.0 International license.

For measuring the size of membrane holes, segmented ER regions were connected in each Z-slice based on connected component analysis and location information. Each of the connected components in a slice was labeled first and its centroid was detected. A 2D matrix was generated that represents pairwise inter-points Euclidean distances of all centroids of ER regions. ER regions were then connected sequentially by utilizing this matrix in a customized breadth first search manner. Specifically, two ER regions having the shortest pairwise distance were selected in the first step. These two regions were connected by a straight line that bridges their nearest boundary pixels. In the second step, previous two regions were used as references to identify a third ER region that has the shortest distance from one of the two references. This region was connected to the closest reference region and taken as the second reference region for next step replacing the reference region it connects with. The connected network was grown gradually in similar fashion by selecting a new region with respect to the two references. One of the references was updated in each step and no region was connected more than twice. Thus, for n number of regions n-1 lines were generated that connects 2 × (n-1) boundary points of the ER regions. After having the list of line coordinates in each Z-slice, we connected lines of subsequent slices that were within proximity of one voxel, resulting in the 3D surface of the holes. The surface area was then quantified, and the diameter was calculated assuming circular shape. The minimal distance measurement, connecting membranes and the surface area measurement were done in MATLAB (The MathWorks Inc., Natick, MA).

Electron tomography

Electron tomography was performed as described in a previous report (Otsuka et al., 2016). Briefly, images were recorded over a -60° to 60° tilt range with an angular increment 1° at a pixel size of 0.75 nm with a TECNAI TF30 transmission EM (TEM; 300 kV; FEI, Hillsboro, OR) equipped with a 4k × 4k Eagle camera (FEI). Tomograms were reconstructed using R-weighted backprojection method implemented in the IMOD software package (version 4.6.40b) (Kremer et al., 1996). For studying interphase NPCs, the cells at >3 h after anaphase onset were examined. For presentation purposes, the image contrast was enhanced by projections of 20 slices (corresponding to 15 nm) for Figs. 2A, B, S2A, S3A, side views in Fig. 4A, and side views in Fig. S8, 8 slices (6 nm) for top views i and iii in Fig. 4A and all the top views in Fig. S8, and 32 slices (24 nm) for top views ii in Fig. 4A. The surface area of the NE analyzed by EM tomography was measured, and the nuclear pore density was calculated as described previously (Otsuka et al., 2016).

bioRxiv preprint doi: https://doi.org/10.1101/141150; this version posted May 23, 2017. The copyright holder for this preprint (which was not certified by peer review) is the author/funder, who has granted bioRxiv a license to display the preprint in perpetuity. It is made available under aCC-BY 4.0 International license.

Membrane profile analysis

For Figs. 2B, S3, the ER and nuclear membranes were manually traced and aligned as described in (Otsuka et al., 2016). The tip-to-tip distance, the ONM/INM distance, and the membrane tip curvature were measured from these two-dimensional profiles in MATLAB 7.4. For the ONM/INM distance, the median of the distance at 50 points between 45 and 90 nm away from the edge of nuclear pores was measured. For the tip curvature, the second derivative of the second-degree polynomial fit at each point along the profile was measured within an arc of 20 nm centered at the apex, and the inverse of the median value was shown as the radius of the tip curvature.

Quantification of dense material within membrane holes

The tomographic subvolume around the membrane hole in the plane of the NE, as indicated by red dashed box in the left panel in Fig. 3A, was Z-projected. Then the radial intensity profile from the center towards the edge was measured using the radial profile plugin in ImageJ. The mean intensity in the region between 57 and 72 nm away from the center was defined as the intensity of the membrane lumen, and used to normalize the intensity in other regions for each membrane hole. The radial intensity profile was measured on 24 nm-Z-projected images for Figs. 3A, S8C, and on 15 nm-Z-projected images for fig. S3B. For measuring inner ring intensity in fig. S8C, the region comprising 80% of the pore radius was regarded as inner ring, and the average intensity of the local 5 nm thick volume was quantified.

Quantification of nuclear surface area growth

HeLa cells stably expressing histone H2b-mCherry were observed by confocal microscopy (LSM780; Carl Zeiss) using 63 × 1.4 NA Plan-Apochromat objective (Carl Zeiss) (Otsuka et al., 2016). Fluorescent chromatin was monitored under the following conditions: 40 optical sections, section thickness of 1.4 μm, z-stacks of every 0.7 μm, the xy resolution of 0.13 μm, and a time-lapse interval of 1 min. The chromosomes were segmented and the surface area was computed as described in (Otsuka et al., 2016). Fluorescence images were filtered with a median filter (kernel size: 0.25 × 0.25 μm) for presentation purposes. Visualization of the chromosome surface in 3D was done in MATLAB.

Seriation of nuclear pores and particle averaging

The subtomograms containing individual pre- and mature pores were extracted and aligned without imposing any symmetry by using the previously described method (Beck et al., 2004).

bioRxiv preprint doi: https://doi.org/10.1101/141150; this version posted May 23, 2017. The copyright holder for this preprint (which was not certified by peer review) is the author/funder, who has granted bioRxiv a license to display the preprint in perpetuity. It is made available under aCC-BY 4.0 International license.

For seriation, the aligned 3D images of individual nuclear pores were resized from 160 × 160 × 120 pixels to 80 × 80 × 60 by averaging neighboring pixels. The whole data set of 399 nuclear pores was then represented by a tensor **A** of dimensions 80 × 80 × 60 × 399. We factorized this tensor into a core tensor **Z** and a set of 4 orthogonal basis matrices U_1, U_2, U_3, and U_4 using a truncated higher order singular value decomposition (HOSVD) (De Lathauwer et al, 2000, Kolda and Bader, 2009) of rank (20,20,15,5):

$$\mathbf{A} = \mathbf{Z} \times_1 U_1 \times_2 U_2 \times_3 U_3 \times_4 U_4,$$

where $\times_n$ represents the mode-n product. HOSVD can be thought of as a form of higher-order principal component analysis with the factor matrices Ui representing the principal components in each mode. U_4 in particular can be seen as containing the coordinates of each nuclear pore on latent axes. From this, we computed the similarity between nuclear pores as $S_{i,j} = 1/(1+D_{i,j})$, where $D_{i,j}$ is the Euclidean distance between pore i and pore j in the space defined by the 5 components of U_4.

Seriation aims at finding a good ordering of items such that similar items are close to each other in the sequence and dissimilar items are further apart or, equivalently, dissimilarities between items increases with their rank difference. This can be formalized using the 2-sum criterion which multiplies the similarity between items by the square of their rank difference. The problem is then to find the optimal ordering that globally minimizes this criterion:

$$\sum_{i,j=n}^{n} S_{i,j}\,(i-j)^2.$$

It has been shown that the optimal order for the 2-sum criterion can be recovered from the sorting order of the Fiedler vector (i.e. the second smallest eigenvector of the Laplacian of the similarity matrix) (Atkins et al, 1998; Ding and He, 2004).

The ordered nuclear pores were sub-clustered into 5 classes with equal Fiedler vector value range (the Fiedler vector value of -1.0 – -0.6, -0.6 – -0.2, -0.2 – 0.2, 0.2 – 0.6, and 0.6 – 1.0 for the clusters 1–5, respectively). The original subtomograms (200 × 200 × 200 pixels) corresponding to the clustered pores were aligned and averaged in each cluster separately without imposing any symmetry by using the previously described method (Beck et al., 2004). For Fig. S8B, pores in individual postmitotic times were selected, aligned, and averaged.

Sample size determination and statistical analysis

For FIB-SEM, we first obtained data from 3 different cells at 3.1, 5.3, and 6.3 min after AO as pilot experiments. After analyzing the chromosome coverage by the NE and nuclear pore number for these three cells, we decided to observe four more cells; three cells at 3.9, 4.3 and

bioRxiv preprint doi: https://doi.org/10.1101/141150; this version posted May 23, 2017. The copyright holder for this preprint (which was not certified by peer review) is the author/funder, who has granted bioRxiv a license to display the preprint in perpetuity. It is made available under aCC-BY 4.0 International license.

5.7 min which are intermediate time points for the NE coverage and pore number increase, and one cell at 11.2 min for the end point (see Fig. 1). For EM tomography, we analysed 5–6 μm^2 NE surface area in each cell at 4.8, 6.1, 10.2 and 15.0 min after AO and in interphase. After quantifying the pre-pore diameter, we analyzed one more cell at 7.7 min which is the intermediate time point for the diameter increase. Exact value of the analyzed surface area and the number of nuclear pores found are listed in Table S2. We picked up all the membrane holes which were visible in the EM tomograms and less than 80 nm in diameter. Since for some pores the membrane contrast was too low to perform membrane profile analysis due to high noise, we excluded them form the quantitative structural analysis and used them only for measuring the pore density in Figs. 2D, S5C. In addition, the nuclear pores near gold particles were removed from the spectral ordering, since the gold particles used for tomography alignment gave high electron density that interfered with the structure-based ordering of those pores. The exact number of pores excluded is also listed in Table S2. For time-lapse 3D imaging in Fig. S5A, B, the data were from two independent experiments. Statistical analyses were performed only after all the data were taken. Statistical analysis methods, sample sizes (N) and P values (P) for each experiment are indicated in figure legends.

Acknowledgements:

We thank the European Molecular Biology Laboratory Electron Microscopy Core Facility; the members of the Ellenberg group and the Beck group for advice and discussion; Anna Kreshuk and Ilya Belevich for help with using Ilastik and MIB, respectively.

Funding:

This work was supported by grants from the German Research Council to J. E. (DFG EL 246/3-2 within the priority program SPP1175), the Baden-Württemberg Stiftung to J.E., and the European Research Council to M. B. (309271-NPCAtlas), as well as by the European Molecular Biology Laboratory (S.O., A.M.S., M.S., J.K.H., M.J.H., S.S., Y.S., M.B., J.E.). S.O. was additionally supported by the EMBL Interdisciplinary Postdoc Programme (EIPOD) under Marie Curie Actions COFUND and a JSPS fellowship (The Japan Society for the Promotion of Science, postdoctoral fellowship for research abroad).

Author contributions:

SO, AMS, YS, MB, and JE designed the project. SO performed quantitative analysis of FIB-SEM data and all the experiments and analyses of EM tomography. AMS acquired all the FIB-

bioRxiv preprint doi: https://doi.org/10.1101/141150; this version posted May 23, 2017. The copyright holder for this preprint (which was not certified by peer review) is the author/funder, who has granted bioRxiv a license to display the preprint in perpetuity. It is made available under aCC-BY 4.0 International license.

SEM data and carried out segmentation of FIB-SEM images. MS contributed to the computational quantitative analysis of EM images. JKH performed spectral ordering. MJH carried out the segmentation of fluorescence images and assisted with computational analysis of EM images. SS helped with the segmentation of FIB-SEM images. YS, MB, and JE supervised the work. SO and JE wrote the paper. All authors contributed to the analysis and interpretation of data and provided input on the manuscript.

References:

Antonin, W., Ellenberg, J. & Dultz, E. Nuclear pore complex assembly through the cell cycle: regulation and membrane organization. *FEBS lett.* **582**, 2004-2016, doi:10.1016/j.febslet.2008.02.067 (2008).

Atkins, J. E., Boman, E. G. & Hendrickson, B. A spectral algorithm for seriation and the consecutive ones problem. *SIAM J. Computing* **28**, 297-310 (1998).

Baum, D. A. & Baum, B. An inside-out origin for the eukaryotic cell. *BMC Biol.* **12**, 76, doi:10.1186/s12915-014-0076-2 (2014).

Beck, M. *et al.* Nuclear pore complex structure and dynamics revealed by cryoelectron tomography. *Science* **306**, 1387-1390 (2004).

Beck, M. & Hurt, E. The nuclear pore complex: understanding its function through structural insight. *Nat. rev. Mol. Cell Biol.* **18**, 73-89, doi:10.1038/nrm.2016.147 (2017).

Belevich, I., Joensuu, M., Kumar, D., Vihinen, H. & Jokitalo, E. Microscopy Image Browser: A Platform for Segmentation and Analysis of Multidimensional Datasets. *PLoS Biol.* **14**, e1002340, doi:10.1371/journal.pbio.1002340 (2016).

Cardona, A. *et al.* TrakEM2 software for neural circuit reconstruction. *PloS one* **7**, e38011, doi:10.1371/journal.pone.0038011 (2012).

Devos, D. P., Graf, R. & Field, M. C. Evolution of the nucleus. *Curr. Opin. Cell Biol.* **28**, 8-15, doi:10.1016/j.ceb.2014.01.004 (2014).

Ding, C. & He, X. Linearized cluster assignment via spectral ordering. *Proceedings of the Twenty-first International Conference on Machine Learning (ICML '04)* pp. 30 (2004).

Dultz, E. *et al.* Systematic kinetic analysis of mitotic dis- and reassembly of the nuclear pore in living cells. *J. Cell Biol.* **180**, 857-865, doi: 10.1083/jcb.200707026 (2008).

Fehrenbach, J., Weiss, P. & Lorenzo, C. Variational algorithms to remove stationary noise: applications to microscopy imaging. *IEEE transactions on image processing* **21**, 4420-4430, doi:10.1109/TIP.2012.2206037 (2012).

Fichtman, B., Ramos, C., Rasala, B., Harel, A. & Forbes, D. J. Inner/Outer nuclear membrane fusion in nuclear pore assembly: biochemical demonstration and molecular analysis. *Mol. Biol. Cell* **21**, 4197-4211, doi:10.1091/mbc.E10-04-0309 (2010).

Kolda, T. G. & Bader, B. W. Tensor Decompositions and Applications, *SIAM Rev.* **51**, 455-500, (2009).

Kremer, J. R., Mastronarde, D. N. & McIntosh, J. R. Computer visualization of three-dimensional image data using IMOD. *J. Struct. Biol.* **116**, 71-76, doi:10.1006/jsbi.1996.0013 (1996).

bioRxiv preprint doi: https://doi.org/10.1101/141150; this version posted May 23, 2017. The copyright holder for this preprint (which was not certified by peer review) is the author/funder, who has granted bioRxiv a license to display the preprint in perpetuity. It is made available under aCC-BY 4.0 International license.

LaJoie, D. & Ullman, K. S. Coordinated events of nuclear assembly. *Curr. Opin. Cell Biol.* **46**, 39-45, doi:10.1016/j.ceb.2016.12.008 (2017).

De Lathauwer, L., Moor, B. D. & Vandewalle, J. A. Multilinear Singular Value Decomposition. *SIAM J. Matrix Anal. Appl.* **21**, 1253-1278 (2000).

Lu, L., Ladinsky, M. S. & Kirchhausen, T. Formation of the postmitotic nuclear envelope from extended ER cisternae precedes nuclear pore assembly. *J. Cell Biol.* **194**, 425-440, doi:10.1083/jcb.201012063 (2011).

Narayan, K. *et al.* Multi-resolution correlative focused ion beam scanning electron microscopy: applications to cell biology. *J. Struct. Biol.* **185**, 278-284, doi:10.1016/j.jsb.2013.11.008 (2014).

Otsuka, S., Szymborska, A. & Ellenberg, J. Imaging the assembly, structure, and function of the nuclear pore inside cells. *Methods Cell Biol.* **122**, 219-238, doi:10.1016/B978-0-12-417160-2.00010-2 (2014).

Otsuka, S. *et al.* Nuclear pore assembly proceeds by an inside-out extrusion of the nuclear envelope. *Elife* **5**, doi:10.7554/eLife.19071 (2016).

Puhka, M., Joensuu, M., Vihinen, H., Belevich, I. & Jokitalo, E. Progressive sheet-to-tubule transformation is a general mechanism for endoplasmic reticulum partitioning in dividing mammalian cells. *Mol. Biol. Cell* **23**, 2424-2432, doi:10.1091/mbc.E10-12-0950 (2012).

Rabut, G., Lenart, P. & Ellenberg, J. Dynamics of nuclear pore complex organization through the cell cycle. *Curr. Opin. Cell Biol.* **16**, 314-321, doi:10.1016/j.ceb.2004.04.001 (2004).

Rotem, A. *et al.* Importin beta regulates the seeding of chromatin with initiation sites for nuclear pore assembly. *Mol. Biol. Cell* **20**, 4031-4042, doi:10.1091/mbc.E09-02-0150 (2009).

Schellhaus, A. K., De Magistris, P. & Antonin, W. Nuclear Reformation at the End of Mitosis. *J. Mol. Biol.* **428**, 1962–85, doi:10.1016/j.jmb.2015.09.016 (2015).

Shibata, Y., Hu, J., Kozlov, M. M. & Rapoport, T. A. Mechanisms shaping the membranes of cellular organelles. *Annu. Rev. Cell Dev. Biol.* **25**, 329-354, doi:10.1146/annurev.cellbio.042308.113324 (2009).

Shimi, T., Butin-Israeli, V. & Goldman, R. D. The functions of the nuclear envelope in mediating the molecular crosstalk between the nucleus and the cytoplasm. *Curr. Opin. Cell Biol.* **24**, 71-78, doi:10.1016/j.ceb.2011.11.007 (2012).

Sommer, C., Straehle, C., Koethe, U. & Hamprecht, F. A. ilastik: interactive learning and segmentation toolkit. *iEEE International Symposium on Biomedical Imaging (ISBI)*, 230-233 (2011).

Ungricht, R. & Kutay, U. Mechanisms and functions of nuclear envelope remodelling. *Nat. Rev. Mol. Cell Biol.* **18**, 229-245, doi:10.1038/nrm.2016.153 (2017).

Walther, T. C. *et al.* The conserved Nup107-160 complex is critical for nuclear pore complex assembly. *Cell* **113**, 195-206 (2003).

Wandke, C. & Kutay, U. Enclosing chromatin: reassembly of the nucleus after open mitosis. *Cell* **152**, 1222-1225, doi:10.1016/j.cell.2013.02.046 (2013).

Weberruss, M. & Antonin, W. Perforating the nuclear boundary - how nuclear pore complexes assemble. *J. Cell Sci.* **129**, 4439-4447, doi:10.1242/jcs.194753 (2016).

bioRxiv preprint doi: https://doi.org/10.1101/141150; this version posted May 23, 2017. The copyright holder for this preprint (which was not certified by peer review) is the author/funder, who has granted bioRxiv a license to display the preprint in perpetuity. It is made available under aCC-BY 4.0 International license.

Supplementary Materials

Figs. S1 to S8
Tables S1 to S2
Legends for Movies S1 to S3

bioRxiv preprint doi: https://doi.org/10.1101/141150; this version posted May 23, 2017. The copyright holder for this preprint (which was not certified by peer review) is the author/funder, who has granted bioRxiv a license to display the preprint in perpetuity. It is made available under aCC-BY 4.0 International license.

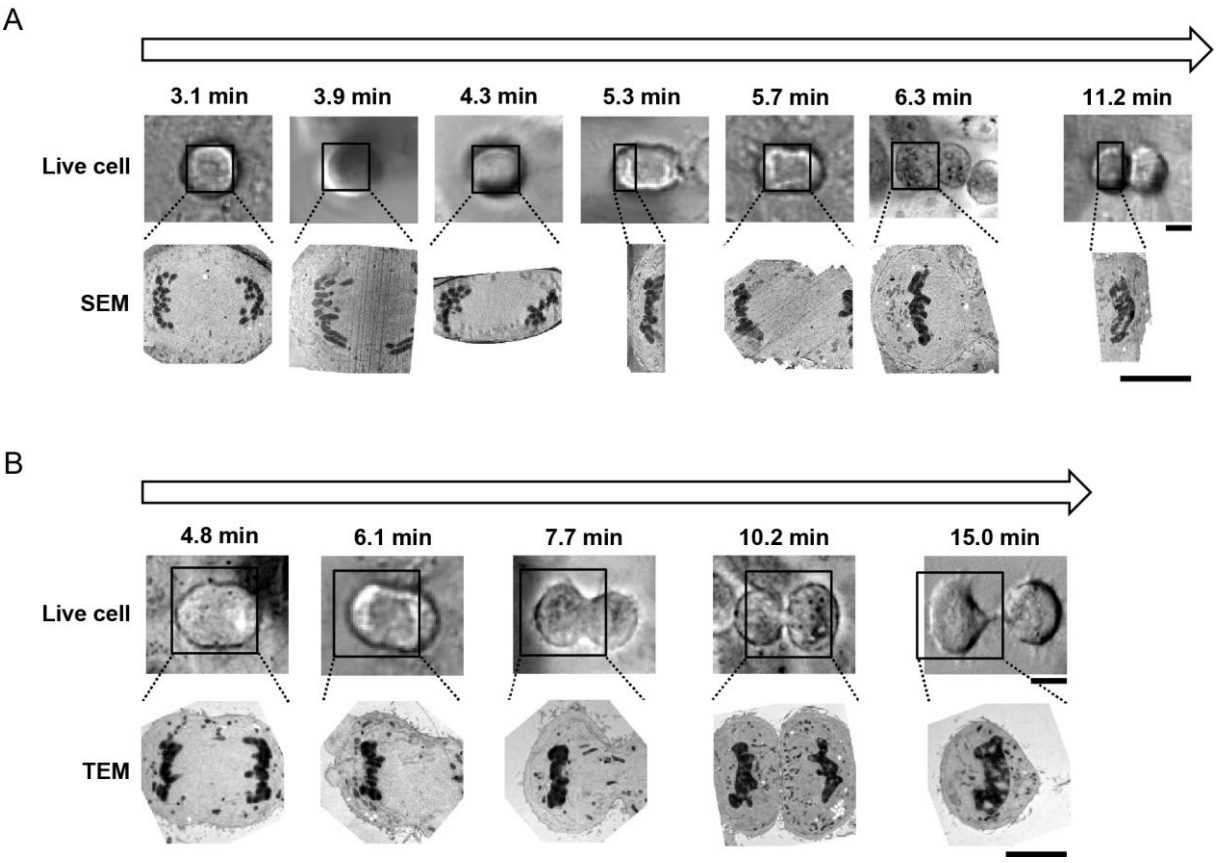

Figure S1. Live-cell and EM images of cells analyzed by FIB-SEM (A) and EM tomography (B). Cells cultured on sapphire disks were imaged by widefield microscopy (upper panels). After high-pressure freezing and plastic-embedding, the same cells were observed by SEM or TEM. The contrast of SEM images shown in (A) are enhanced by projection of a series of 20 images for presentation purposes. TEM images shown in (B) are from one of the serial sections of 300 nm thickness. Time after anaphase onset (AO) is indicated. Scale bars, 10 μm.

bioRxiv preprint doi: https://doi.org/10.1101/141150; this version posted May 23, 2017. The copyright holder for this preprint (which was not certified by peer review) is the author/funder, who has granted bioRxiv a license to display the preprint in perpetuity. It is made available under aCC-BY 4.0 International license.

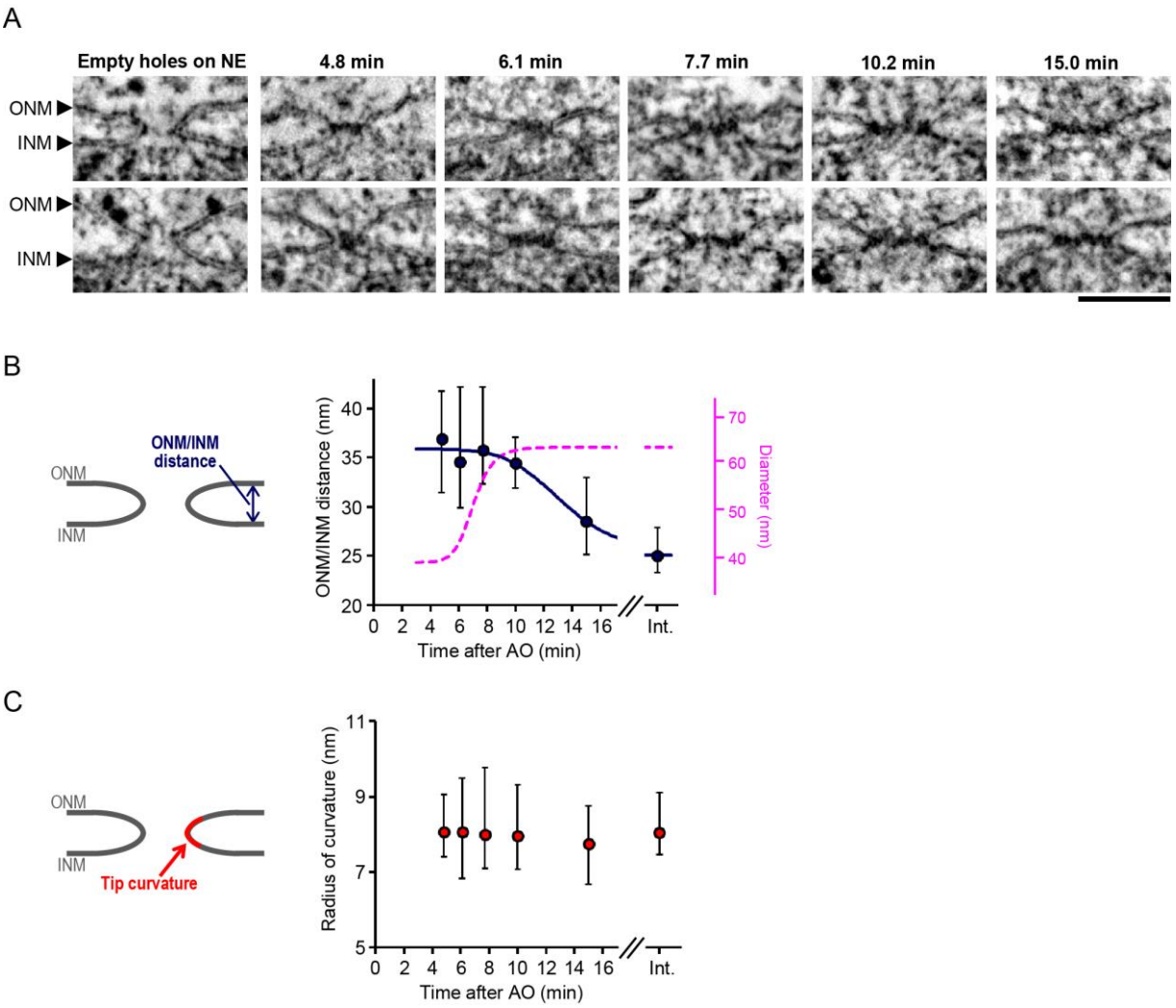

Figure S2. Galleries of postmitotic NPC assembly intermediates and quantification of membrane distance and curvature. (A) Other images of empty holes on chromatin and nuclear pores at different times after AO (4.8, 6.1, 7.7, 10, and 15 min). ONM, outer nuclear membrane; INM, inner nuclear membrane. Scale bar, 100 nm. (B, C) Quantification of the distance between ONM and INM (B) and the radius of membrane tip curvature (C) as indicated by a blue bidirectional arrow and a red arrow in the left panels. The plots of the ONM/INM distance and the tip curvature are from 71, 75, 88, 64, 58, and 52 pores at 4.8, 6.1, 7.7, 10, 15 min, and in interphase, respectively. The median is plotted and the whiskers show the 25th and 75th percentiles. A blue line shows a fitted sigmoid curve. For comparison, a sigmoid curve of pre-pore diameter in Fig. 2C is shown by a pink dashed line. Interestingly, the distance between ONM and INM was very highly variable during early stages of NPC assembly, and became constrained from 36 to 25 nm from 10 min onwards only after pore dilation was completed (B), suggesting that the linker of nucleoskeleton and cytoskeleton (LINC) complex, which connects ONM and INM (Shimi et al., 2012), is established after NPC assembly is completed. On the other hand, the tip curvature of the pre-pore membrane was constant at all time points (C), implying the continuous association of membrane-shaping protein(s) such as reticulons followed by Nups155 and 53 during NPC assembly (Weberruss and Antonin, 2016).

bioRxiv preprint doi: https://doi.org/10.1101/141150; this version posted May 23, 2017. The copyright holder for this preprint (which was not certified by peer review) is the author/funder, who has granted bioRxiv a license to display the preprint in perpetuity. It is made available under aCC-BY 4.0 International license.

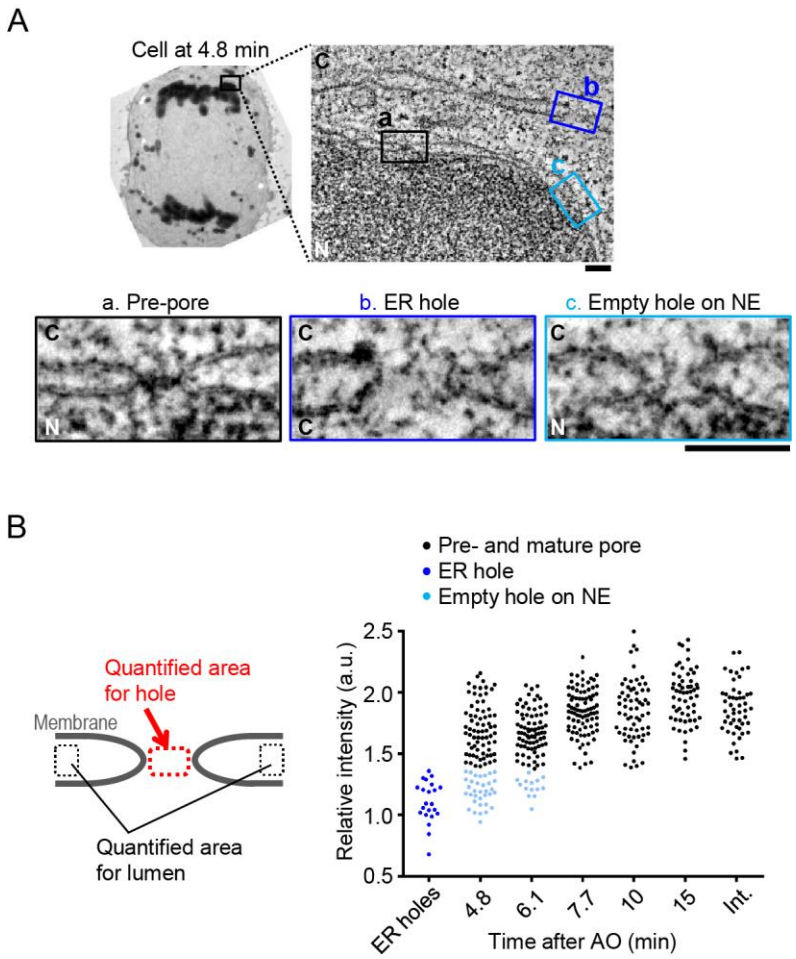

Figure S3. Empty holes with similar diameter to pre-pores on the NE in cells at early time points. (A) An electron tomographic slice of a cell captured at 4.8 min after AO. A pre-pore (a), an ER hole (b), and an empty hole on the NE (c) are indicated by black, dark blue, and light blue boxes, respectively, and their enlarged images are shown in the bottom panels. C, cytoplasm; N, nucleoplasm. Scale bars, 100 nm. (B) Pre-pores can be distinguished from empty holes on the NE by intensity. The intensity in the center of the membrane hole (indicated by a red dotted box in the left panel) was quantified, and the relative intensity to that of the membrane lumen (indicated by black dotted boxes in the left panel) was plotted. The NE holes which have similar intensities to ER holes are regarded as empty holes, and the NE holes which contain higher intensities than ER holes are defined as pre-pores. The diameter of all the empty holes analyzed here is similar to that of pre-pores (20–60 nm).

bioRxiv preprint doi: https://doi.org/10.1101/141150; this version posted May 23, 2017. The copyright holder for this preprint (which was not certified by peer review) is the author/funder, who has granted bioRxiv a license to display the preprint in perpetuity. It is made available under aCC-BY 4.0 International license.

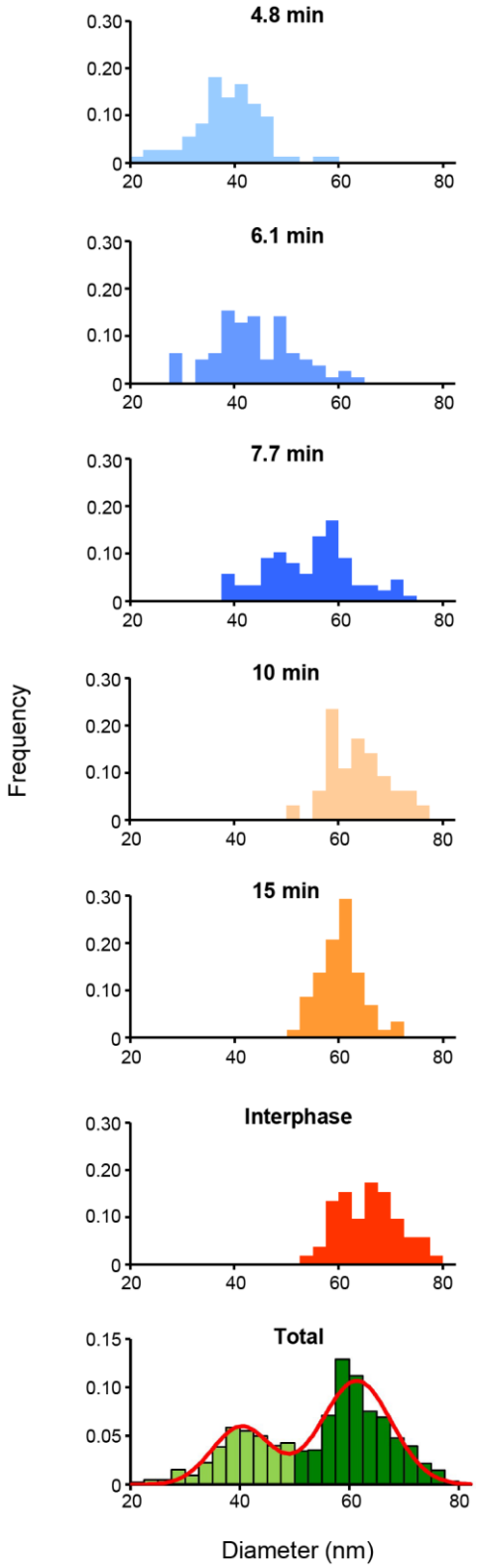

Figure S4. Distribution of nuclear pore diameter measured in Fig. 2B. The diameter of pre- and mature pores at different times after AO is shown in histograms. The diameter of total nuclear pores is also plotted in a histogram and fitted with two Gaussian functions. The intersection of two Gaussians was 51.3 nm, and this value was used to define smaller and larger pre-pores for Fig. 2D.

bioRxiv preprint doi: https://doi.org/10.1101/141150; this version posted May 23, 2017. The copyright holder for this preprint (which was not certified by peer review) is the author/funder, who has granted bioRxiv a license to display the preprint in perpetuity. It is made available under aCC-BY 4.0 International license.

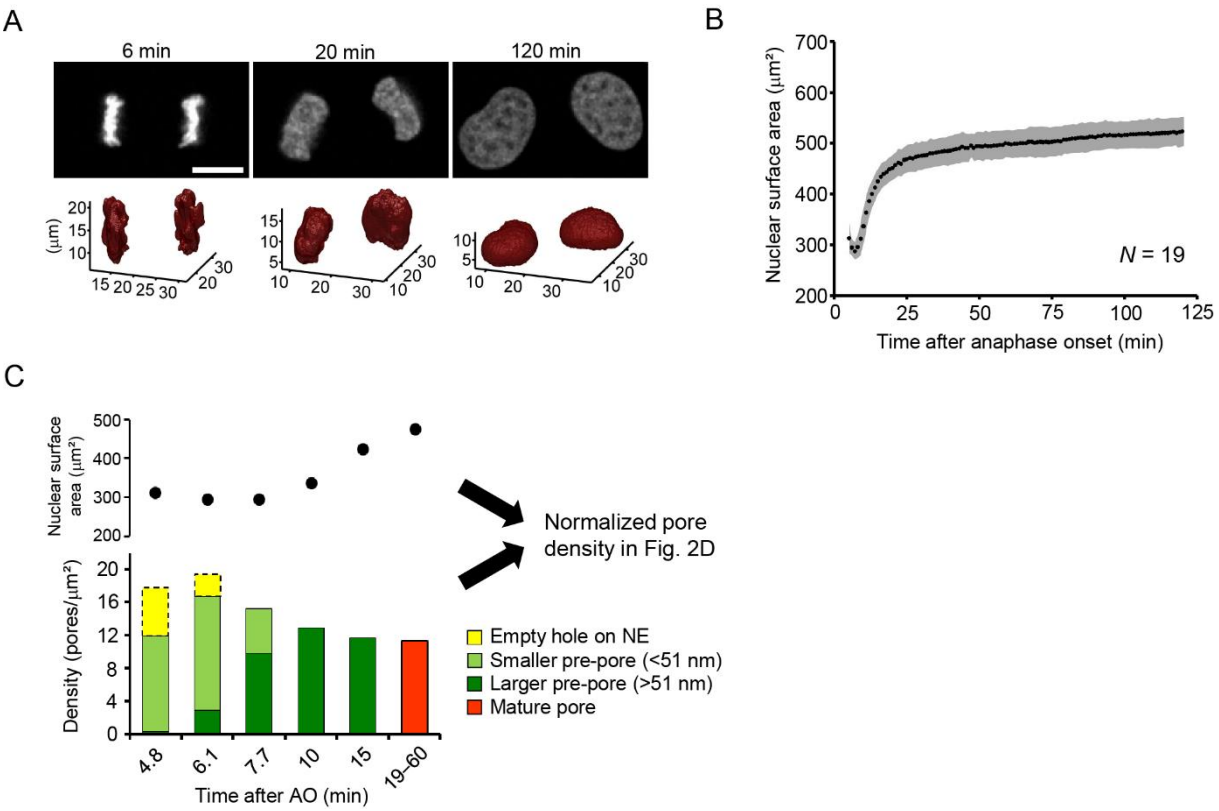

Figure S5. Nuclear surface area measurement for normalizing nuclear pore density. (A) Time-lapse three-dimensional imaging of dividing HeLa cells which express histone-H2b-mCherry. Images show single confocal sections (upper panels) and the segmented nuclei (lower panels) at indicated times after AO. Scale bar, 10 μm. (B) Quantification of nuclear surface area. Black dots and gray lines represent the average and s.d. of measurements from 19 nuclei. (C) The nuclear surface area measured in (A, B) and the density of empty holes on the NE, pre-pores smaller and larger than 51 nm, and mature pores at different times measured by electron tomography (the data are summarized in Table S2). The pores at later than 19 min are defined as mature pores. The pore density at 19–60 min is the average from 6 cells at 19, 24, 28, 36, 42, and 53 min after AO, which was measured previously (Otsuka et al., 2016). The surface area of the nucleus at each time point is plotted above the density histogram. At each time point the density was multiplied by the nuclear surface area to remove the effect of nuclear expansion on the pore density.

bioRxiv preprint doi: https://doi.org/10.1101/141150; this version posted May 23, 2017. The copyright holder for this preprint (which was not certified by peer review) is the author/funder, who has granted bioRxiv a license to display the preprint in perpetuity. It is made available under aCC-BY 4.0 International license.

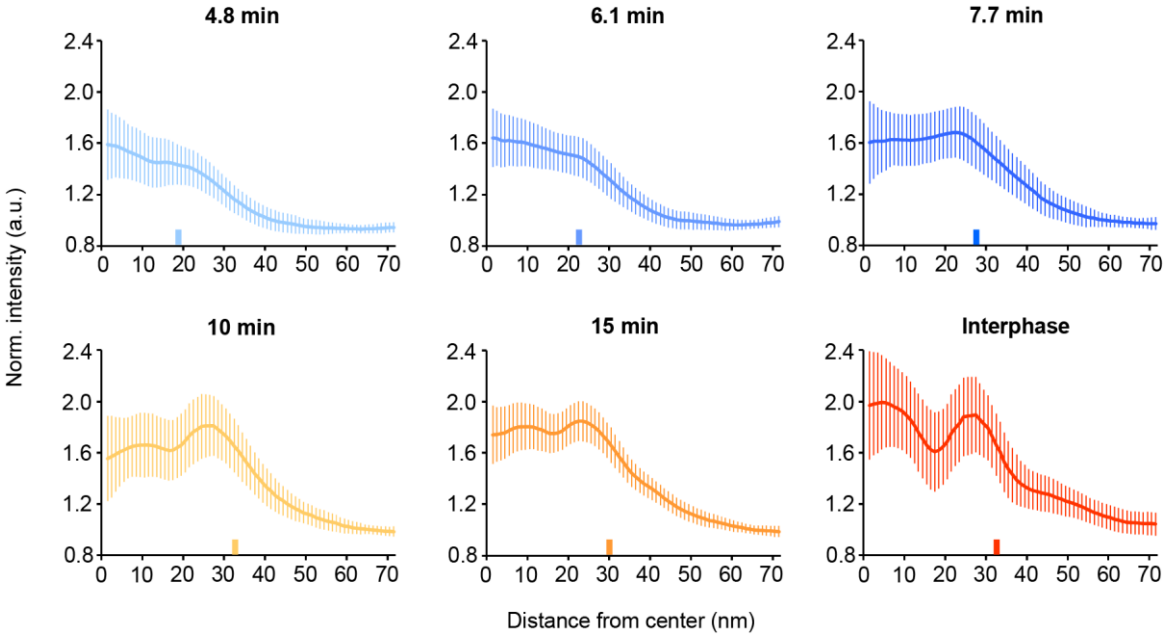

Figure S6. Individual radial profiles of pre-pores shown in Fig. 3A. Bold and fine lines represent the average and s.d. of measurements from 72, 78, 88, 64, 58, and 52 pores at 4.8, 6.1, 7.7, 10, 15 min, and in interphase, respectively. The position of the membrane wall is indicated by a short line on the X-axis for each time point.

bioRxiv preprint doi: https://doi.org/10.1101/141150; this version posted May 23, 2017. The copyright holder for this preprint (which was not certified by peer review) is the author/funder, who has granted bioRxiv a license to display the preprint in perpetuity. It is made available under aCC-BY 4.0 International license.

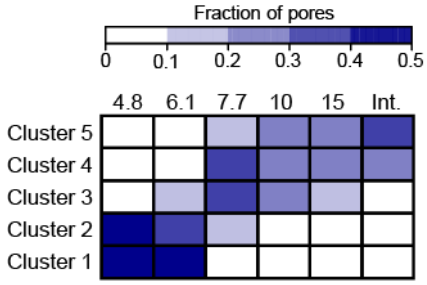

Figure S7. Seriation contingency table. Fraction of nuclear pores at different times after AO is color-coded in each cluster. Cluster 1, 2, 3, 4, and 5 contains the pores at the rank of 1–61, 62–146, 147–215, 216–323, 324–399, respectively.

bioRxiv preprint doi: https://doi.org/10.1101/141150; this version posted May 23, 2017. The copyright holder for this preprint (which was not certified by peer review) is the author/funder, who has granted bioRxiv a license to display the preprint in perpetuity. It is made available under aCC-BY 4.0 International license.

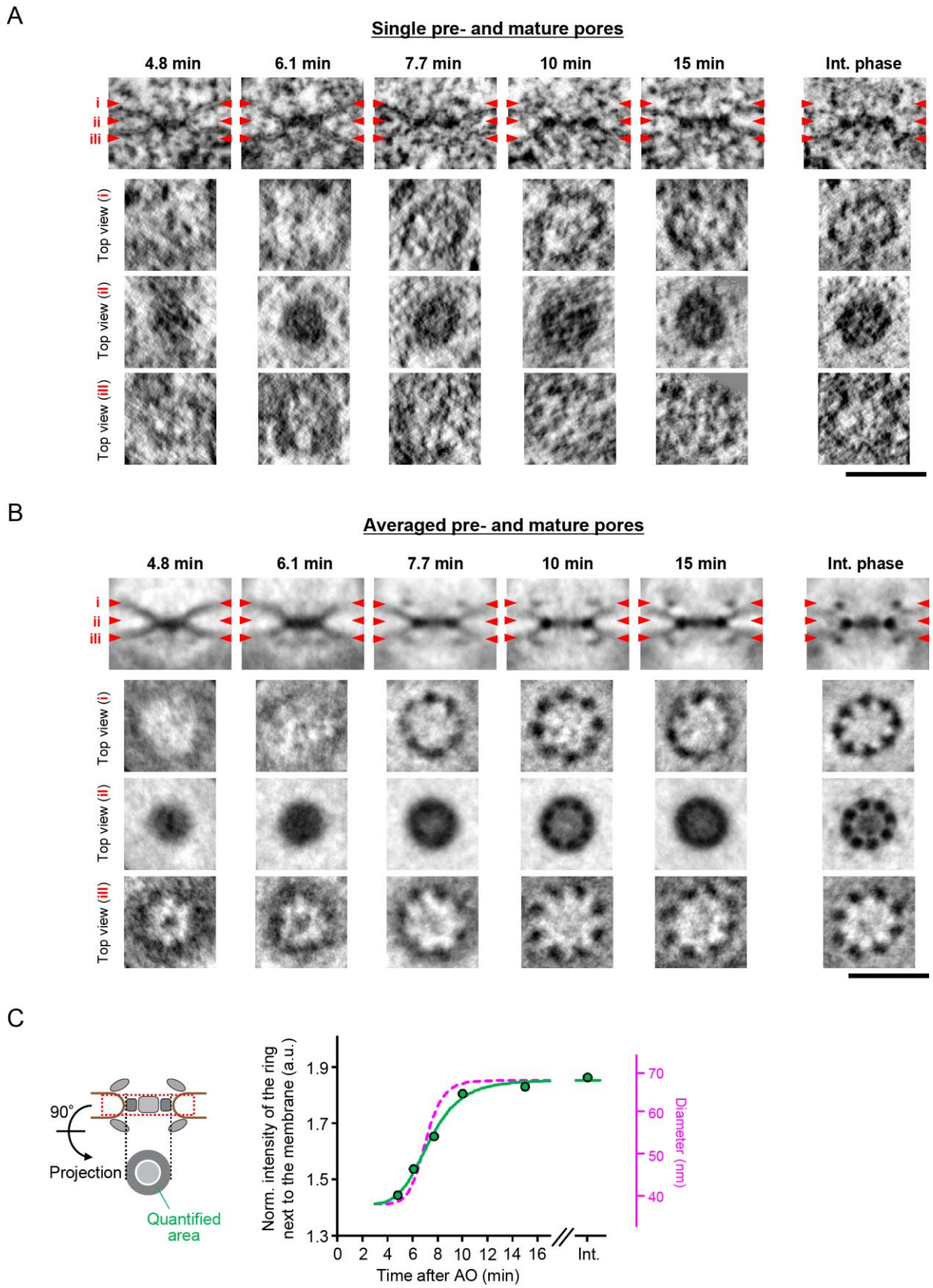

Figure S8. 3D structural comparison of chronologically ordered pre- and mature pores. Electron tomographic slices of single (A) and averaged (B) pre- and mature pores at indicated time points are shown. No symmetry was imposed in averaging. The averaged images are from 72, 78, 86, 64, 58, 52 pores for 3.1, 3.9, 4.3, 5.3, 5.7, and 6.3 min, respectively. Red arrowheads i, ii, and iii on side-view images indicate the locations of the planes which are

bioRxiv preprint doi: https://doi.org/10.1101/141150; this version posted May 23, 2017. The copyright holder for this preprint (which was not certified by peer review) is the author/funder, who has granted bioRxiv a license to display the preprint in perpetuity. It is made available under aCC-BY 4.0 International license.

inclined at 90° in top views i, ii, and iii. Scale bars, 100 nm. (C) Quantification of the inner ring intensity. As in Fig. 3A, the region indicated by red dashed box in the left panel was Z-projected and the radial intensity from the center of the pore was measured. Intensity was normalized to that of NE lumen. The intensity in the region adjacent to the membrane as indicated by a green line in the left panels was quantified and plotted. The plot shows the mean from 71, 75, 88, 64, 58, and 52 pores at 4.8, 6.1, 7.7, 10, 15 min, and in interphase, respectively. A green line shows a sigmoid curve. For comparison, a sigmoid curve of pre-pore diameter in Fig. 2C is shown by a pink dashed line.

bioRxiv preprint doi: https://doi.org/10.1101/141150; this version posted May 23, 2017. The copyright holder for this preprint (which was not certified by peer review) is the author/funder, who has granted bioRxiv a license to display the preprint in perpetuity. It is made available under aCC-BY 4.0 International license.

Time after anaphase onset (min)	3.1	3.9	4.3	5.3	5.7	6.3	11
Chromosome coverage by NE	0.14	0.076	0.087	0.59	0.81	0.88	0.96
Number of nuclear pores	0	0	42	359	1349	1744	2510

Table S1. Summary of correlative single cell live imaging with focused ion beam scanning electron microscopy. A data table shows the chromosome coverage by the nuclear envelope and the number of nuclear pores in cells at indicated postmitotic times.

bioRxiv preprint doi: https://doi.org/10.1101/141150; this version posted May 23, 2017. The copyright holder for this preprint (which was not certified by peer review) is the author/funder, who has granted bioRxiv a license to display the preprint in perpetuity. It is made available under aCC-BY 4.0 International license.

Time after anaphase onset (min)	4.8	6.1	7.7	10	15	*19–60	Int.
Analyzed surface area (μm^2)	6.31	4.85	6.12	5.28	5.22	29.1	5.60
Empty holes on NE	37	13	0	0	0	0	0
Smaller pores than 51 nm	73	67	31	0	0	0	0
Larger pores than 51 nm	2	14	61	68	61	330	56
Pores with high noise	3	3	4	4	3	0	4
Pores near gold particles	3	3	3	0	3	0	0

Table S2. Summary of correlative live imaging with electron tomography. A data table shows the surface area of the NE analyzed by EM tomography in each cell at a different postmitotic time, the number of empty holes on the NE, pores smaller and larger than 51 nm, pores with high noise and with gold particles nearby. The pores with high noise were excluded from the quantitative structural analysis since the membrane contrast was too low for those pores to make membrane profiles, and used only for measuring the pore density in Figs. 2D, S5C. In addition, the pores near gold particles were removed from the spectral ordering, since the gold particles used for tomography alignment gave high electron density that interfered with the structure-based ordering of those pores. *The data at 19–60 min is the sum of 6 cells at 19, 24, 28, 36, 42, and 53 min after AO, which was measured previously (Otsuka et al., 2016).

bioRxiv preprint doi: https://doi.org/10.1101/141150; this version posted May 23, 2017. The copyright holder for this preprint (which was not certified by peer review) is the author/funder, who has granted bioRxiv a license to display the preprint in perpetuity. It is made available under aCC-BY 4.0 International license.

Movie Legends:

Movie S1. Focused ion beam scanning electron microscopy (FIB-SEM) of a whole cell at 6.3 min after anaphase onset. Only 20% of FIB-SEM slices were shown in order to reduce the size of this movie. For full segmentation, the chromosome (light blue), the ER membranes in proximity to the chromosome (dark blue), and pre-pores (yellow) were segmented every 10–15th slices, and the slices in between were interpolated. Scale bar, 2 μm.

Movie S2. Fine segmentation of the nuclear envelope (dark blue) and pre-pores of a part of a cell at 6.3 min after anaphase onset. The pre-pore is indicated by a yellow sphere with the average pre-pore diameter, and the center of the sphere is depicted by a yellow dot. The segmentation was done in every single slices. The upper part shows FIB-SEM images and the bottom part shows the ones with the segmentation. C, cytoplasm; N, nucleoplasm. Scale bar, 1 μm.

Movie S3. Electron tomographic slices of the nuclear envelope of a cell at 7.7 min after anaphase onset. Pre-pores are indicated by pink arrows. C, cytoplasm; N, nucleoplasm. Scale bar, 100 nm.